# Dynamic Core Polarization in High Harmonic Generation from Solids: The Example of MgO Crystals

Liang Li,[1] Yinfu Zhang,[1] Pengfei Lan,[1,*] Tengfei Huang,[1] Xiaosong Zhu,[1]
Chunyang Zhai,[1] Ke Yang,[1] Lixin He,[1] Qingbin Zhang,[1] Wei Cao,[1] and Peixiang Lu [1,2,3,†]

[1]*Wuhan National Laboratory for Optoelectronics and School of Physics, Huazhong University of Science and Technology, Wuhan 430074, China*
[2]*Hubei Key Laboratory of Optical Information and Pattern Recognition, Wuhan Institute of Technology, Wuhan 430205, China*
[3]*CAS Center for Excellence in Ultra-intense Laser Science, Shanghai 201800, China*

Previously, the strong field processes in solids have always been explained by the single-active-electron (SAE) model with a frozen core excluding the fluctuation of background electrons. In this work, we demonstrate the strong field induced dynamic core polarization effect and propose a model for revealing its role in high harmonic generation (HHG) from solids. We show that the polarized core induces an additional polarization current beyond the SAE model based on the frozen cores. It gives a new mechanism for HHG and leads to new anisotropic structures, which are experimentally observed with MgO. Our experiments indicate that the influences of dynamic core polarization on HHG are obvious for both linearly and elliptically polarized laser fields. Our work establishes the bridge between the HHG and the dynamic changes of the effective many-electron interaction in solids, which paves the way to probe the ultrafast electron dynamics.

The ocean tide and atmospheric tide are typical phenomena due to the periodic gravitation variation. In strong laser fields, the bound electrons near the nuclei can also show up tidal motions caused by the periodic laser "pulling," which forms dynamic core (the totality of the nuclei and the bound electrons) polarization. Such polarized cores lead to dynamic changes of the effective Coulomb potential and have non-negligible influences in the interaction of intense laser pulses and solids. In this work, we concentrate on revealing the dynamic core polarization in the high harmonic generation (HHG) from solids.

Recently, solid HHG has attracted much attention for its potential application as a source of extreme ultraviolet radiation [1–5]. It also provides opportunities for crystallographic analysis and probing the electronic properties [6–14], opening a new field of attosecond physics in solids. For all these applications, it is crucial to understand the physics underlying solid HHG. Current investigations are mostly based on the single-active-electron (SAE) time-dependent Schrödinger equation (TDSE) or semiconductor Bloch equations (SBEs) with independent electrons [15–25]. In the TDSE, the interaction between the active electron and core is described by a frozen effective potential (frozen cores) [19–21]. The SBEs [15] model the electron motion in the energy bands, which are obtained from the field-free structure of the solids. In these methods, the many-electron effect is described by the frozen effective potential or by phenomenologically introducing scattering with a constant dephasing time

[4,5]. However, the dynamic changes of the effective many-electron interaction are not included [26–29]. Although *ab initio* simulations can fully include the multielectron effect [30–33], the underlying mechanisms are buried in the wave functions, making it difficult to understand and extract how the dynamic changes of the effective many-electron interaction (i.e., dynamic core polarization) influence the HHG.

In this Letter, we demonstrate that the so-far overlooked dynamic core polarization induced by strong laser fields plays an important role in solid HHG. A quantum trajectory model is proposed, and the dynamic changes of the effective many-electron interaction are involved by introducing a time-dependent effective potential. Our model shows that the polarized core induces an additional polarization current beyond the previous SAE models with frozen cores. It results in new anisotropic structures of the HHG yield: new peaks of anisotropic HHG yields appear in linearly polarized driving fields, and the peaks of anisotropic HHG yields are shifted due to the polarized core in elliptically polarized fields. We also experimentally investigate the anisotropic HHG in MgO with laser fields varying the intensity or ellipticity. The experimental results show remarkable signatures that well support the effect of the polarized core predicted by our theory.

In the framework of Kohn-Sham density functional theory (KS-DFT), a spinless $N$-electron solid system can be described in terms of the one-electron density,

$$\rho(\mathbf{r}) = \sum_{i=1}^{N} |\phi_i(\mathbf{r})|^2, \tag{1}$$

where $\phi_i(\mathbf{r})$ are the KS orbitals that are eigenstates of a one-electron Hamiltonian with KS-potential $v_{\text{eff}}$,

$$\left[ \frac{\mathbf{p}^2}{2} + v_{\text{eff}}(\mathbf{r}) \right] \phi_i(\mathbf{r}) = \epsilon_i \phi_i(\mathbf{r}). \tag{2}$$

The KS potential $v_{\text{eff}}$ can be expressed as

$$v_{\text{eff}}(\mathbf{r}) = \int \frac{\rho(\mathbf{r}')}{|\mathbf{r} - \mathbf{r}'|} d\mathbf{r}' + v_n(\mathbf{r}) + v_{\text{xc}}[\rho(\mathbf{r})]. \tag{3}$$

In Eq. (3), the first two terms are the Coulomb potential of the electrons and nuclei, and the third term is the exchange-correlation potential, which is described by a functional of the electron density.

It is challenging to theoretically model the solid systems interacting with strong laser fields, because both bound electrons and ionized electrons need to be described accurately. Previous models about solid HHG often rely on the SAE assumption [15–25], where only one active electron is mainly influenced by the laser field and the other electrons are treated as frozen. In this case, the dynamics of one electron $\Psi_i(\mathbf{r}, t)$ can be described by the TDSE,

$$i \frac{\partial}{\partial t} \Psi_i(\mathbf{r}, t) = \left[ \frac{\mathbf{p}^2}{2} + v_{\text{eff}}(\mathbf{r}) + H_I(t) \right] \Psi_i(\mathbf{r}, t), \tag{4}$$

$H_I$ is the laser-electron interaction. The effective potential $v_{\text{eff}}(\mathbf{r})$, obtained self-consistently by solving the Eq. (2), remains frozen by using the stationary electron density distribution $\rho_0$. On the basis of Bloch states, one can also deduce the widely used SBEs from Eq. (4), with stationary band structures and transition dipole momenta. Then, the HHG process is explained as follows: an electron is ionized from the parent core and then accelerated by the laser field, accompanied by the generation of induced currents and high harmonics [as shown in Fig. 1(b)]. In this process, the electron, driven by the laser field, is moving under a frozen effective potential, and the dynamic changes of the cores are neglected.

High harmonics are generated with a strong field that is comparable to the electron-binding potential and the bound electrons are generally much less localized in solids compared with those in gases. Therefore, the bound electrons in solids can be pulled back and forth with the strong laser field. In Fig. 1(a), we show the change of the electron density $\rho(\mathbf{r}, t) - \rho_0$ simulated by the time-dependent density functional theory (TDDFT) [37,38]. One can see an obvious fluctuation of the electron density near the core even when the ionization is low (< 0.2%). In this case, the effective potential formed by the polarized cores also changes with time following the laser field. Then, the dynamics of the
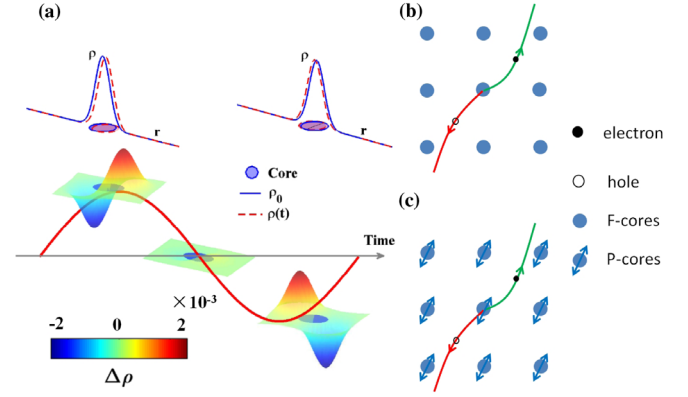


FIG. 1. (a) Upper plots: Sketch of the dynamic core polarization. In the strong laser field, the electron density $\rho$ is modified compared to the initial density $\rho_0$. Bottom plots: the variation of the charge density $\Delta\rho = \rho(t) - \rho_0$ under a linearly polarized laser pulse. The simulation is performed with TDDFT for a model lattice (see section A in the Supplemental Material [34]). $\Delta\rho$ is negligible around the zero points of the electric field. While in the first half cycle, more electrons are pulled to the right side ($\Delta\rho > 0$) by the strong laser field. In the next half cycle, more electrons are pulled to the left side when the electric field changes its sign. (b) The sketch of the trajectory for SAE models. During the acceleration, the electron (hole) is moving under the time-independent potential with frozen cores ($F$ cores). (c) The sketch of the trajectory with polarized cores. In the strong laser field, the electron density changes back and forwards, resulting in the dynamic core polarization. Then, the electron (hole) is moving under the time-dependent potential of polarized cores ($P$ cores).

ionized electron will be influenced when the electron passes the polarized cores and additional polarization current will be induced [as illustrated in Fig. 1(c)]. Note that the core polarization effect has been discussed in atoms or molecules [39,40]. The nonlocalization of electrons and periodic structure can make the core polarization play a different and more significant role in solids, which, however, has not been addressed before.

To model the dynamic core polarization effect, we involve $H_s = v_{\text{eff}}[\rho(t)] - v_{\text{eff}}[\rho_0]$ as a perturbation term of the one-electron Hamiltonian. Then, Eq. (4) is modified as

$$i \frac{\partial}{\partial t} \Psi_i(\mathbf{r}, t) = \left[ \frac{\mathbf{p}^2}{2} + v_{\text{eff}}(\mathbf{r}) + H_I(t) + H_s(t) \right] \Psi_i(\mathbf{r}, t). \tag{5}$$

Considering only a tiny part of electrons is excited ($\Delta\rho \ll 1$), one can solve the Eq. (5) using the perturbation theory for $H_s$ (see section B in the Supplemental Material [34]). The solution, reserving up to the first order of $H_s$, is

$$|\Psi_i(t)\rangle = |\Psi_i^0(t)\rangle + U_0(t, t_0) \int_{t_0}^{t} d\tau U_0^\dagger(\tau, t_0)$$
$$[-i H_s(\tau)] U_0(\tau, t_0) |\Psi_i^0(t_0)\rangle. \tag{6}$$

The first term $|\Psi_i^0(t)\rangle = U_0(t, t_0)|\Psi_i^0(t_0)\rangle$ is the solution of Eq. (4), and $U_0(t, t_0)$ is the time evolution operator satisfying $i(\partial/\partial t)U_0(t, t_0) = [(\mathbf{p}^2/2) + v_{\text{eff}}(\mathbf{r}) + H_I(t)]U_0(t, t_0)$. The second term $|\Psi_i^s(t)\rangle = U_0(t, t_0)\int_{t_0}^t d\tau U_0^\dagger(\tau, t_0)[-iH_s(\tau)]$ $U_0(\tau, t_0)|\Psi_i^0(t_0)\rangle$ comes from the dynamic changes induced by polarized cores. The total current can be expressed

as $\mathbf{J}(t) = \sum_i \langle\Psi_i(t)|\mathbf{p}|\Psi_i(t)\rangle = \sum_i [\langle\Psi_i^0(t)|\mathbf{p}|\Psi_i^0(t)\rangle + \langle\Psi_i^0(t)|\mathbf{p}|\Psi_i^s(t)\rangle + \langle\Psi_i^s(t)|\mathbf{p}|\Psi_i^0(t)\rangle]$. This can be divided into two parts, $\mathbf{J}^0(t)$ and $\mathbf{J}^s(t)$. We evaluate the polarization currents in the framework of quantum trajectories (see section C in the Supplemental Material [34]),

$$\mathbf{J}^0(t) = \sum_i \langle\Psi_i^0(t)|\mathbf{p}|\Psi_i^0(t)\rangle$$

$$= \sum_{t', \mathbf{k}_0 \in BZ} T_{cv}(t')e^{iS_{cv}(t, t')}\mathbf{p}_{cv}[\mathbf{k}(t)]e^{-(t-t')/T_2} + \text{c.c.}$$

$$\mathbf{J}^s(t) = \sum_i [\langle\Psi_i^0(t)|\mathbf{p}|\Psi_i^s(t)\rangle + \langle\Psi_i^s(t)|\mathbf{p}|\Psi_i^0(t)\rangle]$$

$$= \sum_{t', \mathbf{k}_0 \in BZ} \left[\sum_L e^{-i\mathbf{k}(t)\cdot\mathbf{R}_L}\xi(\mathbf{R}_L, t)\right] T_{cv}(t')e^{iS_{cv}(t, t')}\mathbf{p}_{cv}[\mathbf{k}(t)]e^{-(t-t')/T_2} + \text{c.c.} \quad (7)$$

In our simulation, one valence band (VB, denoted as "$v$") and one conduction band (CB, denoted as "$c$") are chosen according to Ref. [19]. The intraband current is omitted due to its minor contribution to the high harmonics above the band gap in the condition of our work [5,21]. $T_{cv}(t')$ is the ionization rate, and $\mathbf{p}_{cv}(\mathbf{k})$ is the transition matrix element between the CB and the VB. $S_{cv}(t, t_i) = \int_{t_i}^t \epsilon_g(\mathbf{k}(\tau))d\tau$ is the dynamic phase. $\epsilon_g$ is the band gap, and $\mathbf{k}(t) = \mathbf{k}_0 + \mathbf{A}(t)$ with $\mathbf{k}_0$ belonging to the first Brillouin zone (BZ), and $\mathbf{A}(t)$ being the vector potential of the laser fields. The isotropic part of the scattering effects is included by introducing the dephasing time $T_2$ [4,5].

In Eq. (7), the first term $\mathbf{J}^0$ is equivalent to the normal current obtained with previous SAE models [19,25] from Eq. (4). The orientation dependence of the corresponding HHG is determined by the scattering with frozen effective potential $v_{\text{eff}}[\rho_0]$. The second term $\mathbf{J}^s$ is contributed by the dynamic core polarization. Different from $\mathbf{J}^0$, an additional anisotropic scattering $\xi(\mathbf{R}_L, t)$ is induced by the dynamic core polarization. This anisotropic scattering can be approximately evaluated by the overlap between the ionized electron and the bound electron wave packet near the core, i.e., $\xi(\mathbf{R}_L, t) \sim e^{-(\mathbf{r}(t)-\mathbf{R}_L)^2/a_{\text{core}}^2}$, where the subscript "core" corresponds to Mg or O and $\mathbf{R}_L$ is the location of cores, and $\mathbf{r}(t)$ is the electron trajectory (see section C in the Supplemental Material [34]). $a_{\text{Mg}}$ and $a_{\text{O}}$ are the sizes of Mg and O cores, respectively. It means that, due to the dynamic core polarization, the ionized electron will be influenced when it passes through the polarized cores. This modifies the current and leads to $\mathbf{J}^s$, which depends on $\xi(\mathbf{R}_L, t)$.

To show how to justify the dynamic core polarization effect on HHG, we discuss HHG from MgO in laser fields varying from linear to circular polarization. The band structure and the transition dipole momenta are obtained

by using the DFT via the Vienna *ab initio* simulation package (VASP) (see Fig. S1 in the Supplemental Material [34]). The band gap energy is 7.8 eV which is much larger than the photon energy of the driven laser (0.95 eV) used in this work. Figure 2 shows the yield of the 17th harmonic as a function of crystal orientation and laser ellipticity as predicted by our model [Figs. 2(a)–2(d) for $\mathbf{J}^s$, and Fig. 2(e) for $\mathbf{J}^0$]. The model also enables us to separate the current and HHG into the contributions from the scattering with different polarized cores. As shown in Fig. 2, all the spectrograms show a spiral structure. For the signal of the nearest-neighbor (NN) Mg and O, see Figs. 2(a) and 2(c), there are four paddles, which correspond to the fourfold symmetry of the atomic configuration. In the linear polarization case, the signal of Mg(NN) peaks along with the bonding directions, e.g., 0°, 90°, while the signal of O(NN) peaks in the middle of each quadrant, e.g., 45°, 135°. With increasing the ellipticity, the peaks of harmonic yields are shifted clockwise away from the bonding directions. Specifically, the Mg(NN) peak moves from 90° to about 45°, and the O(NN) peak moves from 45° to about 25°. Wider paddles can be seen in larger ellipticity until saturation at $\varepsilon \approx 0.5$. In addition, as shown in Figs. 2(b) and 2(d), the signal of the second-neighbor (SN) Mg and O exhibits eight paddles. In the linear polarization case, the harmonic yield peaks at the orientations along the direction from the origin to Mg(SN) and O(SN). In contrast, as shown in Fig. 2(e), the HHG from normal current $\mathbf{J}^0$ (SAE model) exhibits only four paddles peaked at 45° and 135°, etc. Compared with the results of $\mathbf{J}^0$, the polarized-core induced currents can be distinguished by two remarkable signatures: a new anisotropic structure (eight paddles vs four paddles) and different orientation dependence (the locations of the peaks) of HHG [Figs. 2(a)–2(d) vs Fig. 2(e)]. These phenomena can be
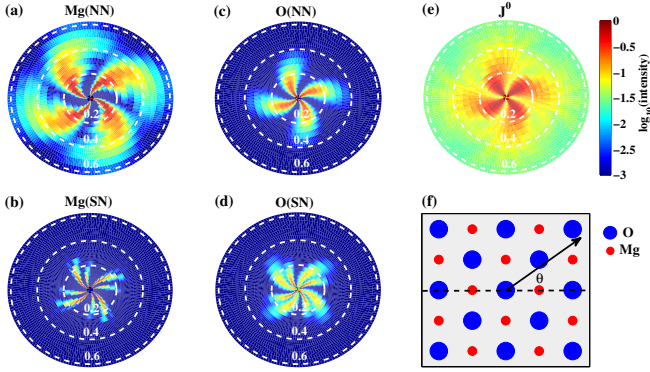
FIG. 2. Orientation dependence of the 17th harmonic yield under different ellipticities contributed by polarized cores of (a) the nearest-neighbor Mg, (b) the second-neighbor Mg, (c) the nearest-neighbor O, (d) the second-neighbor O, and (e) the normal current $\mathbf{J}^0$. (f) The sketch of a ⟨001⟩ cut MgO crystal. $\theta$ indicates the orientation angle between the crystal and the main axis of the laser polarization, and the rotation of polarization is anticlockwise. The radius in (a)–(e) corresponds to the ellipticity, which ranges from $\varepsilon = 0$ to $\varepsilon = 0.63$. The white dashed lines correspond to $\varepsilon = 0.2$, $\varepsilon = 0.4$, and $\varepsilon = 0.6$. The harmonic yields are normalized to 1 in these figures. The wavelength and the intensity of the driving laser are 1300 nm and 5 TW/cm², respectively. The main results will not change for different high harmonics, as one will see in our following discussions about Figs. 3 and 4.

concretely explained by the $\mathbf{R}_L$-dependent terms $\xi(\mathbf{R}_L, t)$. For instance, the eight paddles in Fig. 2(b) are relevant to the Mg(SN) cores, whose locations are $(2a, a)$, $(a, 2a)$, $(-a, 2a)$, $(-2a, a)$, $(-a, -2a)$, $(-2a, -a)$, $(a, -2a)$, and $(2a, -a)$ ($a$ is the lattice constant). These terms are only involved in $\mathbf{J}^s$, and are not predictable by the SAE model (i.e., $\mathbf{J}^0$).

To demonstrate the dynamic core polarization effect, we perform the experiment by using a near-infrared laser, and measure the orientation dependence of HHG with different laser parameters. HHG is generated by focusing a near-infrared laser on the $300 - \mu$m-thick, 001-cut MgO crystal at normal incidence. The near-infrared laser is produced from an optical parametric amplifier (OPA) pumped by an 800-nm, 35-fs (FWHM), 1 kHz laser (Coherent, Astrella-USP-1K). The maximum pump energy is 5 mJ and the maximum output energy is about 600 $\mu$J for the signal and 500 $\mu$J for the idler pulses. The wavelength of the signal pulse of the OPA can be adjusted from 1.2 to 1.6 $\mu$m. We performed the experiment by varying the wavelength and similar orientational dependence of the HHG are observed (see Fig. S3 for additional experimental results in the supplementary materials [34]). The pulse duration measured with an autocorrelator is 100 fs (FWHM) for the signal pulse. The near-infrared laser is focused to a spot of 90 $\mu$m using a lens. We control the laser ellipticity by changing the angle between a half-wave plate and a quarter-wave plate system. The major axis of the elliptical

polarization is fixed during our experiments. High harmonics are detected by a homemade flat-field soft x-ray spectrometer consisting of a flat-field grating (300 grooves/mm) and a slit (with a width of about 0.1 mm and height of 15 mm). The high harmonics passing through the slit are dispersed by the grating and imaged onto the microchannel plate (MCP) fitted with a phosphor screen. The image on the screen is detected by a CCD camera.

We first compare the simulated and experimental results in a linearly polarized laser field. For clarity, we show the lineout of the simulated results from different terms in Fig. 3(a). Only the results from 0° to 90° are shown, considering the fourfold symmetry of the MgO. One can see that the normal current $\mathbf{J}^0$ only contributes a wide peak near 45°. Different from $\mathbf{J}^0$, the currents induced by the dynamic core polarization $\mathbf{J}^s$ predict peaks at 0°, 27°, 45°, 63°, and 90°, contributed by different polarized cores. The experimental results are shown in Fig. 3(b). Note that similar results are also observed for different harmonics (see Fig. S4 in Supplemental Material [34]). One can see three kinds of peaks marked as "$A$" (near 0° and 90°), "$B$" (near 27° and 63°), and "$C$" (near 45°). At lower laser intensity, the peaks "$A$" and "$C$" can be seen, which are also observed in previous experiments [41]. However, with increasing the laser intensity, the peaks "$B$" gradually appear and peak "$C$" in the center between the two peaks "$B$" is less obvious. Although one can not distinguish the contribution of polarized-core induced currents $\mathbf{J}^s$ from "$C$," the contribution of the polarized cores Mg(NN) and Mg(SN) can be clearly identified from "$A$" and "$B$," which is only predicted by $\mathbf{J}^s$. These results indicate that the dynamic core polarization effect plays a non-negligible role in solid HHG. Moreover, the contributions of polarized cores become more obvious with increasing laser intensity. Note that peak $A$ is stronger than that of peak $C$ of the 17th order harmonic. The ratio between peaks $A$ and $C$ becomes smaller with decreasing the harmonic order (see Fig. S4 in
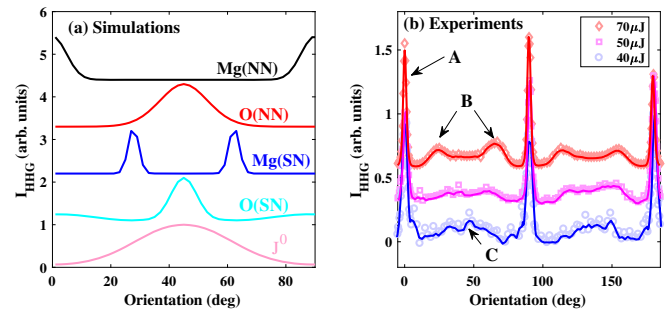


FIG. 3. The orientation dependence of the 17th harmonic yield in the linearly polarized pulse. (a) The simulated results for the contributions of different polarized cores. The lines are normalized to 1, and shifted vertically from each other. (b) The experimental results with different laser power. The lines are normalized and vertically shifted for clarity. The laser powers 40, 50, 70 $\mu$J corresponds to the intensities 3.5, 4.3, 6.0 TW/cm².
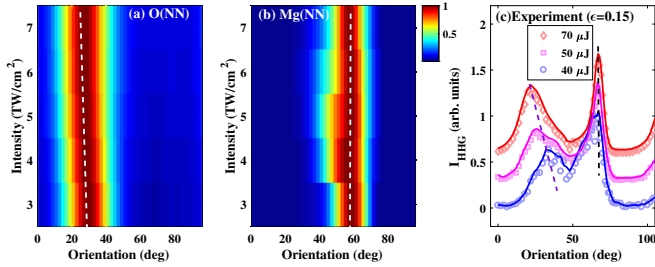
FIG. 4. The orientation dependence of the 17th harmonic yield in elliptically polarized pulse ($\varepsilon = 0.15$). (a) and (b) Simulation results for HHG yields contributed by the O(NN), and Mg(NN) with increasing the laser intensity. (c) The experimental results with different laser power. The lines are normalized and vertically shifted for clarity.

the Supplemental Material [34]). Moreover, the contributions of O(SN) cores are buried by the contribution with other cores, because the electron paths to these cores are hindered by the Mg(NN) cores.

Next, we discuss the case of elliptically polarized laser fields. The simulation and experimental results are shown in Figs. 4(a) and 4(b), and Fig. 4(c), respectively. Similar to discussions about Fig. 3, one can attribute the wide peak at a small angle $\sim 30°$ to the contribution of O(NN) and the narrow peak at $\sim 60°$ to Mg(NN). As shown in Figs. 4(a) and 4(b), the peak contributed by O(NN) shifts from large to small angles with increasing the laser power. This can be intuitively understood by analyzing the electron trajectory (see section D in the Supplemental Material [34]). In contrast, the shift of the peak contributed by Mg(NN) is negligible. These phenomena are supported by the experimental results as shown in Fig. 4(c). Two prominent peaks can be seen within the range from 0° to 90°, and they are shifted following the predictions with increasing the laser intensity. Similar results are also observed for different harmonics, and the shift is reversed for opposite ellipticities (see Figs. S5 and S6 in the Supplemental Material [34]). These phenomena further support our predictions and indicate the dynamic core polarization is also obvious in elliptically polarized laser fields.

In conclusion, our work demonstrates the strong field induced dynamic core polarization, which has been so far overlooked in previous investigations of solid HHG. The new anisotropic structures of HHG yield observed in experiments with MgO clearly indicate the remarkable role of the polarized core. By comparing the theoretical to experimental results, the relation between the atomic configuration and the spectral structure of HHG is revealed. Our work establishes a bridge between the microscopic dynamics and HHG signal, and suggests a potential approach to measure the valence electron density and the field induced charge migration inside the crystals. Although our work only discusses the dynamic core polarization on HHG in MgO, we believe that this effect is general and may be observed in other semiconductors,

insulators, and dielectrics under appropriate laser intensity. The dynamic core polarization will influence the microscopic or even the macroscopic optical and electronic responses. Because the dynamical core oscillates at the frequency of the same order as that of the laser field, it suggests new freedom to control the optical and electronic properties of materials in ultrashort duration.

L. L. and Y. Z. contributed equally to this work.

[*]Corresponding author.
 pengfeilan@hust.edu.cn
 [†]Corresponding author.
 lupeixiang@hust.edu.cn

[1] S. Ghimire, A. D. DiChiara, E. Sistrunk, P. Agostini, L. F. DiMauro, and D. A. Reis, Nat. Phys. **7**, 138 (2011).
[2] H. Kim, S. Han, Y. W. Kim, S. Kim, and S. W. Kim, ACS Photonics **4**, 1627 (2017).
[3] M. Garg, H. Y. Kim, and E. Goulielmakis, Nat. Photonics **12**, 291 (2018).
[4] C. R. McDonald, K. S. Amin, S. Aalmalki, and T. Brabec, Phys. Rev. Lett. **119**, 183902 (2017).
[5] G. Vampa et al., Nat. Phys. **13**, 659 (2017).
[6] B. Zaks, R. B. Liu, and M. S. Sherwin, Nature (London) **483**, 580 (2012).
[7] M. Hohenleutner, F. Langer, O. Schubert, M. Knorr, U. Huttner, S. W. Koch, M. Kira, and R. Huber, Nature (London) **523**, 572 (2015).
[8] F. Langer et al. Nature (London) **533**, 225 (2016).
[9] R. E. F. Silva, I. V. Blinov, A. N. Rubtsov, O. Smirnova, and M. Ivanov, Nat. Photonics **12**, 266 (2018).
[10] T. T. Luu and H. J. Wörner, Nat. Commun. **9**, 916 (2018).
[11] C. Yu, S. Jiang, T. Wu, G. Yuan, Z. Wang, C. Jin, and R. Lu, Phys. Rev. B **98**, 085439 (2018).
[12] T. T. Luu, M. Garg, S. Yu. Kruchinin, A. Moulet, M. Th. Hassan, and E. Goulielmakis, Nature (London) **521**, 498 (2015).
[13] G. Vampa, T. J. Hammond, N. Thire, B. E. Schmidt, F. Legare, C. R. McDonald, T. Brabec, D. D. Klug, and P. B. Corkum, Phys. Rev. Lett. **115**, 193603 (2015).
[14] A. A. Lanin, E. A. Stepanov, A. B. Fedotov, and A. M. Zheltikov, Optica **4**, 516 (2017).
[15] G. Vampa, C. R. McDonald, G. Orlando, D. D. Klug, P. B. Corkum, and T. Brabec, Phys. Rev. Lett. **113**, 073901 (2014).

[16] T. Higuchi, M. I. Stockman, and P. Hommelhoff, Phys. Rev. Lett. **113**, 213901 (2014).

[17] T. T. Luu and H. J. Wörner, Phys. Rev. B **94**, 115164 (2016).

[18] E. N. Osika, A. Chacón, L. Ortmann, N. Suárez, J. A. Pérez-Hernández, B. Szafran, M. F. Ciappina, F. Sols, A. S. Landsman, and M. Lewenstein, Phys. Rev. X **7**, 021017 (2017).

[19] M. Wu, Y. You, S. Ghimire, D. A. Reis, D. A. Browne, K. J. Schafer, and M. B. Gaarde, Phys. Rev. A **96**, 063412 (2017).

[20] M. Wu, S. Ghimire, D. A. Reis, K. J. Schafer, and M. B. Gaarde, Phys. Rev. A **91**, 043839 (2015).

[21] M. Wu, D. A. Browne, K. J. Schafer, and M. B. Gaarde, Phys. Rev. A **94**, 063403 (2016).

[22] T. Ikemachi, Y. Shinohara, T. Sato, J. Yumoto, M. Kuwata-Gonokami, and K. L. Ishikawa, Phys. Rev. A **95**, 043416 (2017).

[23] D. Golde, T. Meier, and S. W. Koch, Phys. Rev. B **77**, 075330 (2008).

[24] T. Y. Du and X. B. Bian, Opt. Express **25**, 151 (2017).

[25] L. Li, P. Lan, X. Zhu, T. Huang, Q. Zhang, M. Lein, and P. Lu, Phys. Rev. Lett. **122**, 193901 (2019).

[26] A. Gordon, F. X. Kärtner, N. Rohringer, and R. Santra, Phys. Rev. Lett. **96**, 223902 (2006).

[27] K. L. Ishikawa and T. Sato, IEEE J. Sel. Top. Quantum Electron. **21(5)**, 1 (2015).

[28] A. A. Romanov, A. A. Silaev, M. V. Frolov, and N. V. Vvedenskii, Phys. Rev. A **101**, 013435 (2020).

[29] M. Abu-samha and L. B. Madsen, Phys. Rev. A **101**, 013433 (2020).

[30] N. Tancogne-Dejean, O. D. Mücke, F. X. Kärtner, and A. Rubio, Phys. Rev. Lett. **118**, 087403 (2017).

[31] N. Tancogne-Dejean, O. D. Mücke, F. X. Kärtner, and A. Rubio, Nat. Commun. **8**, 745 (2017).

[32] D. Bauer and K. K. Hansen, Phys. Rev. Lett. **120**, 177401 (2018).

[33] K. Yabana, T. Sugiyama, Y. Shinohara, T. Otobe, and G. F. Bertsch, Phys. Rev. B **85**, 045134 (2012).

[34] See Supplemental Materials at http://link.aps.org/supplemental/10.1103/PhysRevLett.126.187401 for detail derivation of the theoretical model and additional experimental results, which includes Refs. [35–36].

[35] G. Vampa, C. R. McDonald, G. Orlando, P. B. Corkum, and T. Brabec, Phys. Rev. B **91**, 064302 (2015).

[36] U. Birkenheuer, J. C. Boettger, and N. Rösch, J. Chem. Phys. **100**, 6826 (1994).

[37] E. Runge and E. K. U. Gross, Phys. Rev. Lett. **52**, 997 (1984).

[38] X. Andrade et al., Phys. Chem. Chem. Phys. **17**, 31371 (2015).

[39] B. Zhang, J. Yuan, and Z. Zhao, Phys. Rev. Lett. **111**, 163001 (2013).

[40] S. G. Walt, N. Bhargava Ram, M. Atala, N. I. ShvestovShilovski, A. von Conta, D. Baykusheva, M. Lein, and H. J. Wörner, Nat. Commun. **8**, 15651 (2017).

[41] Y. S. You, D. A. Reis, and S. Ghimire, Nat. Phys. **13**, 345 (2017).